# In--flight performance of the MAMA detectors on the Space Telescope Imaging Spectrograph

Randy A. Kimble[*a], James Abraham[b], Vic S. Argabright[b], Ralph C. Bohlin[c], Richard Bybee[b], Edward Culver[b], Anthony C. Danks[d], Steven Franka[b], Ronald L. Gilliland[c], Charles L. Joseph[e], Mary Elizabeth Kaiser[f], Don J. Lindler[g], Chris A. Long[c], Richard A. Shaw[c], Max Styonavich[b], J. Gethyn Timothy[h,i], Charles N. Van Houten[b], and Bruce E. Woodgate[a]

[a]Code 681, Goddard Space Flight Center, Greenbelt, MD 20771
[b]Ball Aerospace and Technologies Corporation, Boulder, CO 80306
[c]Space Telescope Science Institute, 3700 San Martin Drive, Baltimore, MD 21218
[d]Raytheon ITSS/Code 681, Goddard Space Flight Center, Greenbelt, MD 20771
[e]Rutgers University, Department of Physics and Astronomy, Piscataway, NJ 08855
[f]Johns Hopkins University, Department of Physics and Astronomy, Baltimore, MD 21218
[g]Advanced Computer Concepts/Code 681, Goddard Space Flight Center, Greenbelt, MD 20771
[h]Centre for Research in Earth and Space Science, York University, Toronto, Ontario M3J 1P3, Canada
[i]Nightsen, Inc., 30 Fresno Road, Warwick, RI 02886-1407

## ABSTRACT

The Space Telescope Imaging Spectrograph (STIS) is a versatile HST instrument covering the 115-1000 nm wavelength range in a variety of spectroscopic and imaging modes. Coverage of the ultraviolet range (115-310 nm) is provided by two Multi-Anode Microchannel Array (MAMA) detectors built by Ball Aerospace. The FUV MAMA covers the 115-170 nm range using an opaque CsI photocathode on the microchannel plate; the NUV MAMA covers the 165-310 nm range using a semi-transparent $Cs_2Te$ photocathode on the detector window. Both MAMAs utilize a $1024 \times 1024$ anode format, but detected photon events are positioned to half the spacing of the anode lines, leading to a $2048 \times 2048$ format for the final readout. The active area of each detector is $25.6 \times 25.6$ mm.

Since the installation of STIS onto the Hubble Space Telescope (HST) in February 1997, the MAMAs have carried out a varied program of astronomical observing and in-flight calibration. The detectors have performed extremely well. In this report, we briefly describe the design of the STIS MAMA detectors, provide illustrative examples of their scientific use on HST, and summarize their technical performance in orbit, in such areas as sensitivity, resolution, flat-field uniformity and stability, signal-to-noise capability, dynamic range, and background.

**Keywords:** detectors, ultraviolet, microchannel plate, MAMA, space instrumentation, spectroscopy, HST

## 1. INTRODUCTION

The Space Telescope Imaging Spectrograph (STIS) is a versatile, broadband (115-1000 nm), second-generation spectrograph and imager for the Hubble Space Telescope. It was designed and developed to replace and greatly expand on the capabilities of two first generation HST instruments, the Goddard High Resolution Spectrograph and the Faint Object Spectrograph. In February 1997, STIS was installed in the focal plane of the HST during the HST Second Servicing Mission. Descriptions of the design of STIS and its initial in-flight performance are provided by Woodgate et al.[1] and Kimble et al.[2], respectively.

The large advances offered by STIS over previous HST observing capabilities stem primarily from the use of large format two-dimensional array detectors. Coverage of the 305-1000 nm range is provided by a $1024 \times 1024$ pixel, backside-thinned, UV-enhanced CCD developed by Scientific Imaging Technologies. Coverage of the 115-310 nm range is provided by two photon-counting Multi-Anode Microchannel Array (MAMA) detectors built by Ball Aerospace. Their two dimensional

[*] Correspondence — Email: kimble@ccd.gsfc.nasa.gov; Telephone: 301-286-5783; Fax: 301-286-1752

formats offer imaging spectroscopy (long-slit and slitless), medium and high resolution echelle spectroscopy with wide simultaneous wavelength coverage, and HST's first efficient solar-blind UV imaging capability. In this report, we briefly describe the design of the STIS MAMA detectors, provide illustrative examples of their scientific use on HST, and highlight key aspects of their performance in orbit to date.

### 1.1. MAMA Design Overview

The STIS MAMAs are sealed tube microchannel plate (MCP) detectors; the "MAMA" nomenclature denotes the coupling of the MCP gain stage to a particular form of coded anode array readout. These detectors combine solar-blind, low-background, photon-counting capability with large-format, high-spatial-resolution imaging. Performance advantages of the technology include geometrically stable imaging and high global dynamic range (by virtue of the digital nature of the readout) as well as high local dynamic range and extended count lifetime (by virtue of the relatively low MCP gain required compared with alternative analog readout systems). More detailed descriptions of general MAMA concepts and technology are provided by Timothy and coworkers[3-5]; details of the design, development, and pre-flight performance of the STIS MAMAs specifically have been reported by various members of the STIS team.[6-11] See (1) for a complete table of pre-flight performance metrics.

Each detector consists of an entrance window ($MgF_2$), a photocathode (CsI or $Cs_2Te$), a curved-channel microchannel plate (C-plate), and an anode array. The components are held in a hermetic, stacked Kovar and ceramic body that is indium-sealed to the $MgF_2$ window in the front and welded to a Kovar flange on a multilayer ceramic header at the back. The multilayer ceramic header provides support and electrical connections to the coded anode array outputs. High voltage connections are made to the annular Kovar rings.

At the input to the detectors, the two MAMAs differ slightly in design. For the far ultraviolet (115-170 nm), the FUV MAMA employs a CsI photocathode deposited directly onto the MCP; a field electrode ("repeller") is provided to direct photoelectrons produced by the MCP web back toward the MCP pores (with a field strength of -180 V/mm). The field electrode may be turned off to improve spatial resolution at the expense of quantum efficiency; though characterized in ground test, this operating mode has not yet been implemented in flight. For the near ultraviolet (165-310 nm), the NUV MAMA employs a $Cs_2Te$ photocathode deposited on the inside of the detector window. Photoelectrons generated by the photocathode are proximity focussed to the MCP with a voltage of -700 V across the 0.23 mm window-to-MCP gap.

The curved channel MCPs have an active area of $28 \times 28$ mm embedded in a 40 mm diameter circular glass disk. The MCPs have 12 μm pores on 15 μm centers with an l/d ratio of 120/1. Voltages of -2250 V and -2050 V are applied across the C-plates of the FUV and NUV MAMAs, respectively, yielding modal gains of $7 \times 10^5$ electrons per event; the event pulse height distributions have a FWHM to modal gain ratio of <40%.

The anode arrays are of the type known as "fine-fine" arrays[12], with 1024 anode lines and 66 associated charge amplifiers in each axis; the anode lines are spaced by 25 μm. Valid photon events are those which deposit sufficient charge on two to six adjacent anode lines (in each axis) to drive the associated charge amplifiers above their discriminator thresholds simultaneously. High speed ASIC decode electronics determine the unique event location corresponding to the particular combination of amplifiers. If non-contiguous anode lines are simultaneously excited, no valid event position is found in the ASIC lookup table, and the event is rejected. This feature is particularly valuable for rejecting Cherenkov photons produced essentially simultaneously by the passage of energetic particles through the detector windows (a process that produced the dominant on-orbit background in the HST first-generation spectrographs' Digicon detectors).

Though the anode lines are fabricated in a $1024 \times 1024$ array, event addresses are read out in a $2048 \times 2048$ format by assigning events that excite an even number of anode lines (two, four, or six) to positions corresponding to halfway between the central pair of lines in the event.[13] This "high-res" readout mode (the default for acquisition and downlink of STIS data) offers the finest sampling ($12.5$ μm $\times$ $12.5$ μm pixels) available for STIS spectroscopy or imaging, though with much larger flat-field non-uniformity and somewhat reduced flat-field stability compared to the $1024 \times 1024$ "low-res pixel" format. The impressive resolution achievable in the high-res readout mode is described in Section 3.3.

## 2. SAMPLE MAMA OBSERVATIONS

The principal scientific observing modes enabled by the two-dimensional format of the MAMA detectors are 1) first-order imaging spectroscopy (long slit or slitless), 2) medium or high resolution echelle spectroscopy with wide simultaneous wavelength coverage, and 3) solar-blind UV imaging. In addition, any of these observing modes may be combined with

high-time-resolution (128 μsec) time-tag readout of the detected photon events, if desired for monitoring of time variable sources. (The standard readout mode, with a higher global event rate capability [280,000 counts/second vs. 30,000], is to acquire and downlink accumulated spectra or images rather than individual photon events, always in the 2048 × 2048 format.)

A wide variety of resolving powers and observing apertures are available for UV spectroscopy with the MAMAs, as well as a modest complement of filters for UV imaging. See (1) for details. In this section, we briefly cite a few examples of how the MAMA observing capabilities may be used.

### 2.1 First Order Imaging Spectroscopy

First order imaging spectroscopy can be carried out over 25-30 arcsecond fields of view, with HST-limited spatial resolution (60-100 milli-arcseconds). Published applications of this capability to the investigation of spatially extended astronomical objects include the detection of high velocity Ly α emission in the SN1987A supernova remnant[14], and the study of the velocities and ionization conditions in the circumnuclear clouds of the Seyfert galaxy NGC4151[15].

Another powerful use of the imaging spectroscopy capability is highlighted in Figure 1[16]. In this case, the goal is the measurement of the distribution of singly ionized helium in the high-redshift intergalactic medium, through spectroscopy of the z = 3.286 quasar Q 0302-003 in the far ultraviolet. While the source in this case is not spatially extended, it is extremely faint, and the two-dimensional imaging spectroscopy format is crucial for permitting an accurate subtraction of the sky (airglow) and internal detector backgrounds.

### 2.2 Echelle Spectroscopy

Medium and high resolution echelle spectroscopy modes are provided in both MAMA bands, with nominal spectral resolving powers of 46,000 and 30,000 in the medium resolution mode (for the FUV MAMA and NUV MAMA, respectively) and 110,000 in the high resolution mode. The two-dimensional detectors record numerous spectral orders of the echelle formats, yielding simultaneous wavelength coverage ranging from 20-35 times that of corresponding modes of the GHRS first generation HST spectrograph.

As for first order spectroscopy, the two-dimensional format is also invaluable for enabling accurate background subtraction in observations of faint sources. For brighter sources, the visibility of the full echelle format permits detailed modelling and subtraction of grating-scattered light (particularly strong for the FUV echelles), permitting the determination of accurate line profiles.

Astrophysical applications range from spectroscopy of relatively nearby stars within our own galaxy to observations of distant quasars. The measurement of numerous absorption features in the wideband spectra provides a powerful probe of the physical conditions in the interstellar medium (ISM) or intergalactic medium (IGM) along the observed line of sight. An example of a high signal-to-noise, single orbit observation of a bright Milky Way star in the FUV high resolution echelle mode is shown in Figure 2.

### 2.3 Solar-Blind Ultraviolet Imaging

As astronomical sources are often many orders of magnitude brighter in the visible than in the ultraviolet, the strong visible light rejection of the MAMA detectors is important even in many spectroscopic applications; for ultraviolet imaging, it is absolutely crucial. The sensitive, solar-blind imaging provided by the STIS MAMA detectors is unique on HST. The CCDs of WFPC2 have moderate quantum efficiency in the ultraviolet; however, they must observe through low transmission Woods filters to yield a clean ultraviolet bandpass. Coupled with CCD read noise and dark current, the resulting sensitivity is much lower than offered by the STIS solar-blind, photon-counting MAMAs.

Beautiful STIS FUV MAMA images of the aurorae of Jupiter and Saturn have been widely publicized[17,18] (complete with time-resolved movies enabled by the time-tag readout mode). Here we highlight a UV imaging example from a bit farther afield. Figure 3 presents an NUV MAMA image of the nearby galaxy M32. This image, the deepest UV image ever taken of M32, detects individual hot horizontal branch stars, resolving for the first time the stars that make the dominant contribution to the long-mysterious UV upturn in the spectra of elliptical galaxies.[19]

## 3. TECHNICAL PERFORMANCE

In this section, we summarize the in-flight performance of the STIS MAMA detectors with respect to some key parameters. For further details we refer the interested reader or potential STIS user to the references cited and to documentation maintained by the Space Telescope Science Institute, such as the STIS Instrument Handbook.[20]

### 3.1 Resets of the Detector Control Electronics

Soon after launch and installation into HST, it was discovered that the reset circuitry in the control electronics for both the MAMA and CCD detectors on STIS showed an unforeseen response to radiation-induced transients produced in optical-isolator components in the electronics chain. Because of this sensitivity, energetic particles (encountered primarily in the South Atlantic Anomaly [SAA]) can cause a partial reset of the detector electronics, abruptly shutting down the high voltage for the MAMA detectors.

For the CCD, reconfiguration of the detector control voltages (all <35 V) at each SAA exit is a sufficient and benign approach for dealing with the issue. For the MAMAs, which operate at >2 kV, it is preferable neither to cycle the high voltage rapidly around each SAA crossing, nor to leave the high voltage on and suffer abrupt shutdowns daily. Instead, the MAMAs are operated in the following manner. Each MAMA's high voltage is ramped up and down at the nominal slow rate just once per day in the block of contiguous non-SAA-crossing orbits, if the MAMA is scheduled for use that day. This regimen restricts MAMA availability to 40-45% of HST orbits, adequate for scheduling the planned MAMA science. No deleterious effects of this daily voltage cycling have been observed.

The resets are unrelated to the MAMA technology itself and are easily correctable in future designs. Simple filtering to remove the "hair-trigger" response of the reset circuitry to the optical-isolator transients should prevent this problem for the future HST instruments ACS and COS, both of which will fly spare STIS MAMA detectors as part of their detector complement.

### 3.2 Sensitivity

The quantum efficiencies of the STIS detectors as measured in pre-flight calibration are shown in Figure 4. The QE's plotted for the MAMA detectors are for the tubes as a whole, including the transmission of the detector windows. The peak value of 25% for the FUV MAMA (including window) is quite respectable; the peak value of 10% for the semi-transparent $Cs_2Te$ NUV MAMA was somewhat disappointing.

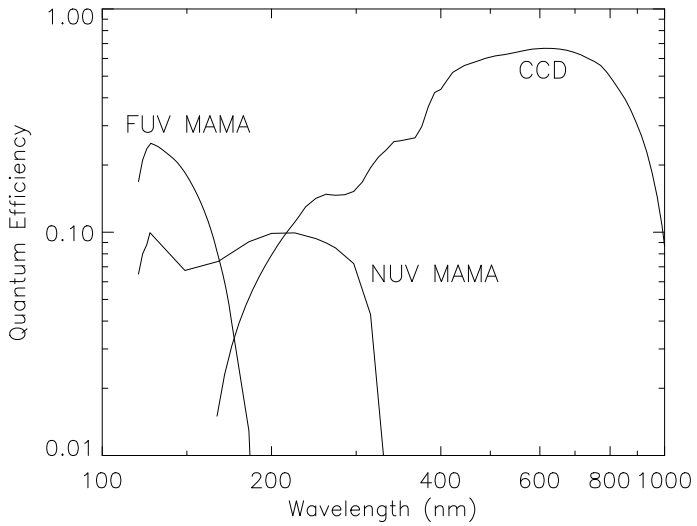


Figure 4. Pre-flight quantum eficiencies of the STIS detectors.

Detector efficiencies can not be measured directly in flight. However, the end-to-end throughput of the HST/STIS combination is in good accord with pre-flight expectations. What can be measured very accurately in flight is the stability of the HST + STIS response. Regular monitoring of standard stars in the low resolution spectroscopic modes demonstrates that

the end-to-end throughput has been extremely, but not perfectly, stable.[21] Averaged over wavelength, the throughput of the FUV low resolution mode appeared to decline by 0.8% per year over the time period from June 1997 to October 1998, though that band-averaged decline was only detected at the 2.3σ level. More statistically significant declines of ~1.5-2% per year were derived for wavelength bins at the 115 nm and 165 nm ends of the band. As there are six reflecting optics in the optical path for this observing mode (two HST + four within STIS), it is quite plausible that this small decline is related to slight contamination of the optics and not the FUV MAMA detector. It should be noted that the temporal slope of the FUV response was derived after correction for an apparent dependence of the detector response on its operating temperature. The slope derived for that correlation was -0.37% per degree C.

The NUV MAMA low resolution spectroscopic mode, in contrast, showed an apparent *increase* in sensitivity over the same time period with a slope of ~1.5% per year throughout the bandpass. It is hard to attribute the change to the optical components in this case. A broadband increase in optical reflectivity is difficult to produce, and a STIS/CCD mode with overlapping wavelength coverage and several optical elements in common with the NUV MAMA mode does not show the same increase. We speculate that some slow evolution in the $Cs_2Te$ photocathode may be the cause.

### 3.3 Resolution

Like the sensitivity, the spatial resolution of the MAMA detectors can not be cleanly separated from the end-to-end performance of the HST + STIS combination once in flight. However, internal calibration lamp exposures indicate that the resolution performance of STIS itself is unchanged from pre-flight calibration, and overall, the end-to-end spectral/spatial resolution performance is in good agreement with pre-flight expectations. The top level optical performance of STIS in-flight has been reviewed by Bowers et al.[22] We highlight key aspects here.

STIS UV spectroscopic modes are generally specified to deliver FWHM resolutions of ~2.3 low-res pixels (~60 μm; 60-70 milli-arcseconds depending on the mode) when observing through a uniformly illuminated 2-pixel-wide slit. The FWHM resolution of the detector PSF's alone (~25 and ~30 μm for the FUV and NUV MAMAs, respectively, in low-res readout mode) is sufficient to support this, as long as the optical aberrations are small. Slit-limited observations of stellar spectra and internal calibration lamp exposures demonstrate that this specification is being met in-flight. When observations are not slit-limited at the two-pixel width (e.g. when wider slits are used, or when evaluating the cross-dispersion resolution for long-slit exposures), then the effective resolution broadens to as much as 3-4 low-res pixels in the FUV, as small angle scatter broadens the intrinsic HST PSF at the shortest ultraviolet wavelengths.

It is interesting to evaluate what resolution the MAMA detectors are capable of delivering when pushed to their limits. The observation of HD210839 by Jenkins shown in Figure 2 represents such a limiting case. The nominal spectral resolving power for the FUV high resolution echelle mode of that exposure is 110,000 for two low-res pixel illumination. However, that exposure was taken through the narrowest available STIS aperture (25 milli-arcseconds, projecting to just one *high-res* pixel with the substantial anamorphic demagnification by the echelle grating in that mode). Furthermore, the target star was near the orbital pole during the observation, rendering orbital Doppler smearing of the spectrum negligible (onboard Doppler correction can only correct the shift to the nearest high-res pixel). The resulting absorption line profiles are remarkably narrow. Figure 2b, provided by Ed Jenkins, plots the FWHM of the absorption lines in high-res pixels vs. their strength. The widths of the weaker, unsaturated lines cluster in the neighborhood of two high-res pixels. This corresponds to a net FWHM resolution of 25 μm and a spectral resolving power of ~200,000. This represents the highest spectral resolving power ever achieved on an astronomical target in this wavelength range and is an impressive demonstration of the MAMA performance.

### 3.4 Flat Field Uniformity and Stability

Flat-field uniformity and stability are key attributes of the MAMA technology. The geometric stability of the readout and the relatively low MCP gain of operation (minimizing sensitivity changes with accumulated exposure) should yield the stability of response necessary for carrying out high S/N work. This is particularly crucial for a spectrograph; accurate flat-fielding is critical to quantitative analysis of (and even for assessing the reality of) apparent absorption lines in an observed spectrum. In this section and the following, we demonstrate that the positive expectations for the MAMA detectors in this regard are being realized in flight.

Figure 5 presents the in-flight pixel-to-pixel flat field for the FUV MAMA detector in the $1024 \times 1024$ low-res pixel format. This so-called "P-flat" (generated by R. Shaw of STScI from in-flight calibration lamp exposures) is created by removing the low-spatial-frequency response of the detector to yield the high-spatial-frequency pixel-to-pixel response array. (For the

FUV MAMA, the low-frequency variations are +/-10%; the NUV MAMA response is remarkably smooth on broad spatial scales, with rms variations <1%.[23])

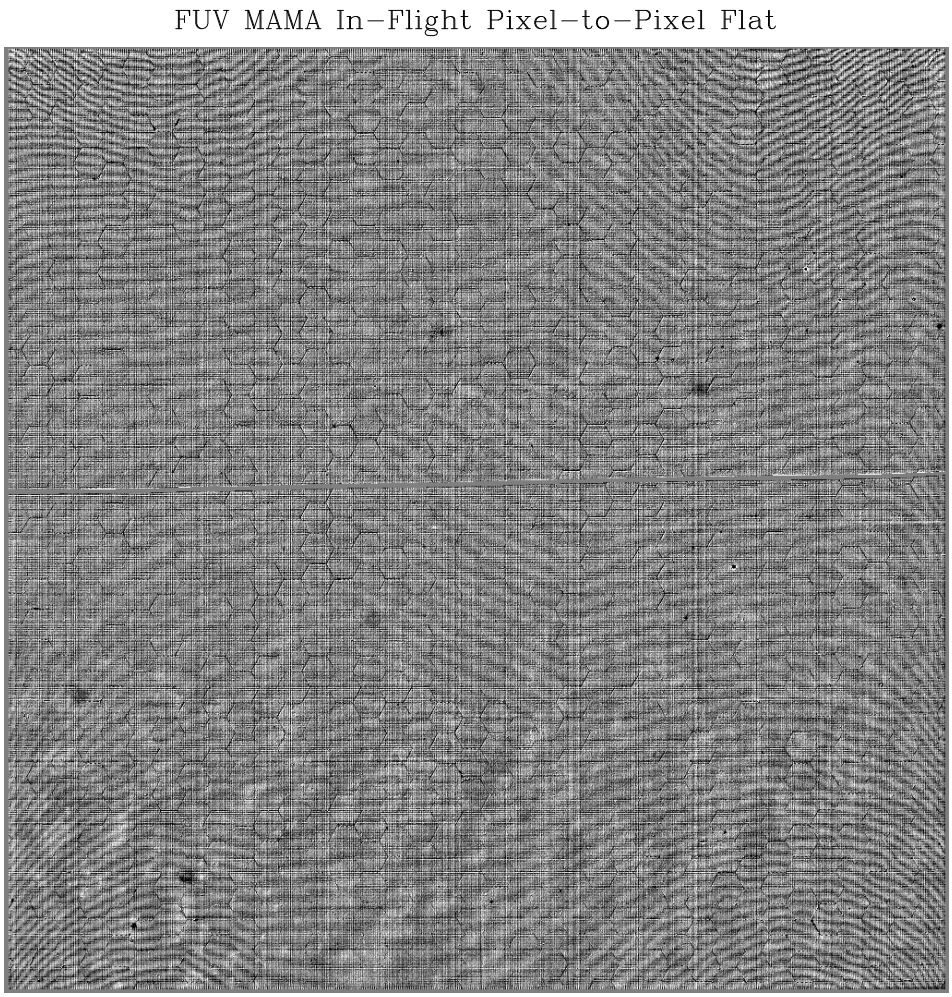


Figure 5. FUV MAMA pixel-to-pixel flat derived from in-flight calibration exposures. The flat field array is highly stretched in the display, with the full grey-scale range corresponding to a flat field response range of 0.92 to 1.08.

Three principal features are seen in the pixel-to-pixel flats (the NUV MAMA flat is similar, with slightly smaller rms variations): horizontal and vertical stripes that result from non-uniformities in the anode array and amplifiers, the standard hexagonal pattern inherent to MCP detectors due to the pore processing methodology, and a Moire pattern that presumably results from the beating of the MCP pore spacing against the spacing of the anode lines. The rms variations in this FUV P-flat are 4.0%; in the corresponding NUV MAMA P-flat, the rms variations are 3.1%.

In the high-res 2048 $\times$ 2048 format, rms variations are very much greater: 42% and 56% for the FUV and NUV MAMAs, respectively. This is not surprising: no matter how uniform the response of the detector, there is no a priori reason that the number of two-four-and six-fold events should equal the number of three-and-five fold events in any particular region of the detector. The relative frequency of the even-fold and odd-fold events depends on the MCP pulse height distribution and on the precise alignment of the MCP pores to the anode lines locally.

The stability of the MAMA flat fields can be assessed by comparing the flats created in-flight with flats generated during pre-launch calibration. Differences in these could be associated with launch shifts or the effects of the detector's integrated exposure between the flat-field calibration periods. Table 1 presents the ratios of the in-flight to pre-flight P-flats for the two

detectors on three spatial scales: at the high-res pixel level, at the low-res pixel level, and at the $2 \times 2$ pixel nominal resolution element level.

Table 1. RMS Variations in Ratio of In-Flight P-Flat to Pre-Flight P-Flat

| Detector | per high-res pixel | per low-res pixel | per $2 \times 2$ pixel res element |
|---|---|---|---|
| FUV MAMA | 6-11% | 1.8% | 1.0% |
| NUV MAMA | 4% | 1.4% | 0.7% |

The changes in the flat-field from pre-launch to in-flight are extremely low at the low-res pixel and resolution element scale; a significant portion of these small differences can be attributed to the statistical errors in the production of the respective flats. The high-res flat field changes appear to be real, however, and are likely attributable to very small shifts in the MCP-to-anode alignment through launch.

In assessing the likely stability of the flat-field response through continuing years in orbit, it is important to evaluate whether there is any sign that the accumulated exposure seen by the MAMA detectors thus far is contributing to the flat-field changes observed. In addressing this question, we make use of the accumulated MAMA images maintained by STScI; daily summed and cumulative count images are available for both detectors. To look for signs of sensitivity loss due to integrated illumination, we plot the in-flight/pre-flight flat-field ratio vs. integrated exposure level. A significant slope in this correlation would be an indication that the accumulated counts were affecting the flat-field response.

Figure 6 presents the results of this check, based on the cumulative counts through May 3, 1998. As the integrated exposure levels are smooth on the $2 \times 2$ pixel scales, we plot the comparison on that scale to reduce the statistical scatter. No significant trends are seen. (The comparison can not be made with more recent data, as the in-flight flats were created from calibration exposures in the May 1998 timeframe. When new calibration flats are obtained later this year, more sensitive stability checks comparing in-flight flats and greater total count doses will be possible.)

Note that this null result is completely expected; any other result would be cause for alarm. Pre-flight life testing by V. Argabright of Ball Aerospace indicated that, for these well-scrubbed, low-gain MCPs, 1% response changes should not be expected until $\sim 5 \times 10^7$ counts per low-res pixel are extracted from the plates[11], far in excess of the current exposure levels. Note also that periodic shifting of the position of first order spectra on the MAMA detectors helps to keep the integrated local exposures down; from May 1998 through June 1999, the total dose on the MAMA detectors increased by a factor of five (to $\sim 2.3 \times 10^{10}$ counts for each detector), but the peak local dose increased by only a factor of two.

### 3.5 Signal-to-Noise Capability

By virtue of the flat-field stability described above, both MAMA detectors have demonstrated outstanding performance in the critical parameter of signal-to-noise capability. In-flight evaluation of the MAMA high S/N capability is described in detail by Kaiser et al.[24] We briefly summarize here. The formal STIS S/N specification is that the instrument shall deliver a S/N capability of >100 per $2 \times 2$ pixel resolution element, count statistics permitting. In-flight tests have demonstrated that single, low resolution spectra can be rectified to this level or better, for both detectors, using composite flats constructed from ground-based calibration data. Orbital Verification tests have yielded S/N ~130 for the FUV MAMA and ~150 for the NUV MAMA for spectra reduced in this way. The flat-fields that have now been constructed from in-flight data may improve the rectification of MAMA spectra further.

In the higher resolution echelle modes, Doppler shifting of the spectrum over the detector (due to the orbital motion of HST) smooths the detector response and improves the flat-fielding even more. Combining the Doppler smoothing with spectral offsetting techniques analogous to the F-P split methodology employed by the GHRS and the FOS, STIS has demonstrated S/N capability of 280 per spectral resolution element for the FUV MAMA (Figure 7a) and 340 per spectral resolution element for the NUV MAMA (Figure 7b) in echelle mode observing.[24]

### 3.6 Dynamic Range

Another key feature of the MAMA detectors is the wide dynamic range they provide. As for other photon counters, their lack of read noise is a strong advantage in lengthy observations of faint sources, providing excellent limiting sensitivity. Despite the higher-than-expected background rates encountered in flight (see Section 3.7), this feature has been well

demonstrated in astronomical observing with the STIS MAMAs. For example, FUV MAMA observations of the Hubble Deep Field South[25] yield 3-4 σ detections of compact galaxies with total count rates of ~$1 \times 10^{-3}$ $s^{-1}$. (The observing time for this field was 52,124 seconds.) With a FWHM of 3-4 pixels for unresolved objects in FUV imaging, this corresponds to peak local count rates of ~$1 \times 10^{-4}$ $pixel^{-1}$ $s^{-1}$ for these statistically significant detections.

At the other extreme, the MAMAs provide significantly higher global and local count rate capability than typical photon counters. This is crucial in enabling the high signal-to-noise potential of the MAMAs (described above) to be achieved in practical observing times. The MAMA event decode electronics have an effective deadtime of ~290 nsec, yielding an intrinsic global count rate capability of 350,000 cts $s^{-1}$ at 10% rolloff. In STIS, counts from the MAMA tubes are FIFO-buffered and stored in image memory; with the flight electronics this process is essentially lossless up to a count rate of ~280,000 cts $s^{-1}$, with a sharp falloff at higher input rates. The effective maximum rate capability in flight is thus ~280,000 cts $s^{-1}$, with ~8% non-linearity at that limiting rate.

It is important to note that the resolution and signal-to-noise capability are not affected at high global count rates. The high S/N echelle spectra presented in Figure 7 were obtained at count rates of 225,000 and 100,000 cts $s^{-1}$ for the FUV and NUV MAMAs, respectively. The total integration times were 13,600 seconds (spread over seven orbits) each to obtain those spectra with S/N ~ 300/1. Similarly, the echellogram shown in Figure 2, for which the limiting resolution of two *high-res* pixels was demonstrated, was obtained at a count rate of 108,000 cts $s^{-1}$. (The brighter orders of that spectrum also achieved 1% count statistics per nominal spectral resolution element (2 *low-res* pixels wide) in that 1506 second integration, which took less than one orbit.)

Because of the low gain of operation, the MAMA tubes offer high local count rate capability as well. The 10% rolloff points for local count rate are 225 and 340 cts $pixel^{-1}$ $s^{-1}$ for the FUV and NUV tubes, respectively, extremely high compared with higher-gain analog readout systems. For various reasons (higher sensitivity change per count at high input rates; details of operation of the on-board count rate safety monitoring), the Space Telescope Science Institute enforces a screening limit of 100 cts $pixel^{-1}$ $s^{-1}$ in pre-observation planning; targets with higher predicted local count rates will not be observed. For imaging of compact sources, this is the effective operational limit (rather than the global count rate); for spectroscopy, the global count rate screening limits of 200,000 cts $s^{-1}$ for echelle spectroscopy and 30,000 cts $s^{-1}$ for first-order spectroscopy almost always come into play before the local rate limit. However, all of these cases represent a wide dynamic range for the detectors; they indicate the ability to carry out observations of a wide range of targets and fields, and the potential for high signal-to-noise observations in practical observing times.

### 3.7 Backgrounds

The only MAMA performance parameters that have not met pre-flight expectations are the detector dark rates. Detector backgrounds on the ground for both tubes ran at 6 cts $s^{-1}$ (1 $cm^{-2}s^{-1}$; $6 \times 10^{-6}$ $pixel^{-1}$ $s^{-1}$). In flight, both background rates have increased markedly.

The FUV MAMA background now ranges from the pre-flight level of 6 cts $s^{-1}$ to as high as 50 cts $s^{-1}$. Because the dark rate correlates strongly with detector temperature (Figure 8c), and the mean operating temperature of the detector has been increasing, the typical detector background rate encountered during an FUV MAMA observation has been increasing with time since launch (Figure 8b). The enhanced background is not spatially uniform, but localized on the detector (Figure 8a). While the peak rate is still quite low ($1.4 \times 10^{-4}$ $pixel^{-1}$ $s^{-1}$), the spatial non-uniformity and temporal variability can make the background difficult to subtract accurately, especially in observations of extended, low-surface-brightness sources.

The FUV MAMA dark enhancement phenomenon was observed on the ground at high temperatures, where it was observed to correlate with both the tube temperature and the time since high voltage turnon. It is known that, when present, the enhancement is strongly affected by the repeller voltage, in the sense that it increases with the magnitude of that voltage. Nonetheless, the precise physical mechanism is not understood.

The dark rate of the NUV MAMA is much more uniform spatially, but because it is so much greater (1000-2000 cts $s^{-1}$), it is much more problematic. The high dark level of the NUV MAMA detector is an unfortunate consequence of long time-constant phosphorescence in the detector's $MgF_2$ window after excitation of metastable states during SAA crossings. While this potential concern was well known to the STIS team before launch, an error in the screening of this particular $MgF_2$ ingot allowed a window with a high concentration of phosphorescent impurities to be used on the flight tube. The per-pixel dark rate is still relatively modest (1-2 $\times$ $10^{-3}$ $pixel^{-1}$ $s^{-1}$). Hence, short exposures utilizing the full resolution capability of the

MAMA are not affected. However, observations that are long or that rely on substantial binning of the signal in the analysis are significantly compromised by the higher-than-expected background.

Significant amelioration of both detectors' dark rate problems is expected after the installation of the Aft Shroud Cooling System (ASCS) in HST Servicing Mission 3b. The primary purpose of the ASCS (which will connect capillary pump cooling lines from the detector interfaces to an external radiator) is to maintain the STIS and ACS detectors in their nominal operating temperature ranges despite gradual warming of the HST aft shroud. However, the reduction of the MAMA operating point by >10 C will have extremely beneficial affects on the detector background rates as well. The FUV MAMA should operate thereafter in a temperature range in which the localized dark enhancement is never present. Likewise, modelling of the temperature dependence of the NUV MAMA dark rate[26] indicates that cooling of the NUV MAMA tube could reduce the steady-state dark rate by roughly a factor of 2 and could periodically reduce the dark rate by more than a factor of 10 over a several day period in an active "boiloff─cooling" campaign mode. Such reductions will be extremely beneficial for some key STIS observing programs, especially in extragalactic astronomy.

### 3.8 Detector Health

No indications of degradation in the health of the MAMA tubes or electronics have been observed. All engineering telemetry values have been stable, including the critical high voltage settings and currents. The occasional abrupt high voltage turnoffs due to spacecraft safing events or particle-induced resets outside of the SAA have shown no apparent effect (nor were they expected to). As indicated in Section 3.4, there is no sign of localized loss of response due to cumulative illumination.

One useful evaluation of internal health of the MAMA tubes is provided by performing what is known as a "fold analysis". The "fold" count of an event is the number of anode lines/amplifiers driven above threshold by the charge pulse. The total fold count for valid events thus ranges from four to twelve (two to six in each axis; see Section 1.1). As the number of amplifiers excited is directly related to the size of the charge cloud impinging on the anode array, the relative frequency of the various fold values thus serves as a rough measure of the pulse height distribution of the events emerging from the MCP.

Fold analysis measurements of the MAMA tube have been carried out roughly twice per year since 1996 (pre-launch). Illumination is provided by internal calibration lamps. Special commands to the flight software are used to set the ASIC decode chip event counters to respond only to events with particular total fold values. After cycling through the various possibilities, a frequency histogram can be derived. Loss of gain in the MCP would be indicated by a systematic shift toward lower fold values, while gassiness in the tube would be revealed by an increase in the fraction of large or saturated pulses. As indicated in Figure 9, no significant trends in the fold distributions for the tubes have yet been seen.

## 4. SUMMARY

The MAMA detectors of the Space Telescope Imaging Spectrograph have been operating in space at the focal plane of the Hubble Space Telescope for over two years. They support a varied program of ultraviolet imaging spectroscopy, medium and high resolution echelle spectroscopy with wide simultaneous wavelength coverage, and solar blind imaging. Overall performance of the detectors has been excellent, with stable sensitivity, high spatial/spectral resolution, stable flat-field response, wide dynamic range, and demonstrated high signal-to-noise capability.

Particle-induced resets of the detector control electronics have reduced the duty cycle over which the MAMAs are available for observing; these resets are unrelated to the MAMA detector technology itself. The only intrinsic detector performance characteristics that have not met pre-flight expectations are the detector backgrounds, with a thermally-induced background excess seen in the FUV MAMA, and substantial window phosphorescence in the NUV MAMA. Both of these backgrounds should be significantly ameliorated when the detector operating temperatures are lowered after the connection of capillary pump cooling lines to STIS in HST Servicing Mission 3b. The health of both MAMA tubes appears to be excellent, indicating that they should capable of supporting a rich astronomical observing program with HST/STIS for years to come.

## ACKNOWLEDGMENTS

We are grateful to all whose efforts over many years made the development of the STIS MAMA detectors successful. We also thank Sally Heap, Ed Jenkins, and Tom Brown for making sample STIS observations available for this publication. The STIS Investigation Definition Team has been funded in response to NASA Announcement of Opportunity OSSA-4-84 through the *Hubble Space Telescope* Project at Goddard Space Flight Center. This paper is based on observations with the

NASA/ESA *Hubble Space Telescope*, obtained at the Space Telescope Science Institute, which is operated by AURA, Inc., under NASA contract NAS5-26555.

## REFERENCES


1. B. E. Woodgate et al., "The Space Telescope Imaging Spectrograph Design," *PASP* **110**, pp. 1183-1204, 1998.
2. R. A. Kimble et al., "The On-Orbit Performance of the Space Telescope Imaging Spectrograph," *ApJ* **492**, pp. L83-L93, 1998.
3. J. G. Timothy, "Optical Detectors for Spectroscopy," *PASP* **95**, pp. 810-834, 1983.
4. J. G. Timothy and R. L. Bybee, "High-resolution pulse-counting array detectors for imaging and spectroscopy at ultraviolet wavelengths," *Ultraviolet Technology*, *Proc. SPIE* **687**, pp. 109-116, 1986.
5. J. G. Timothy, J. S. Morgan, D. C. Slater, D. B. Kasle, and R. L. Bybee, "MAMA detector systems: a status report," *Ultraviolet Technology III*, *Proc. SPIE* **1158**, pp. 104-117.
6. A. C. Danks, C. Joseph, R. Bybee, V. Argabright, J. Abraham, R. Kimble, and B. Woodgate, "The STIS MAMA status: current detector performance," in *Proceedings of an ESA Symposium on Photon Detectors for Space Instrumentation (ESA SP-356)* (Noordwijk: ESA/ESTEC), pp. 269-274, 1992.
7. C. L. Joseph, V. S. Argabright, R. L. Bybee, A. Danks, and B. E. Woodgate, "Test and evaluation of the space telescope imaging spectrograph (STIS) engineering model units of the MAMA detectors," *Ultraviolet Technology V*, R. E. Huffman & C. G. Stergis, eds., *Proc. SPIE* **2282**, pp. 116-125, 1994.
8. C. L. Joseph, V. S. Argabright, J. Abraham, D. Dieball, S. Franka, M. Styonavich, C. Van Houten, A. Danks, B. E. Woodgate, "Performance results for the STIS flight MAMA detectors," *Photoelectronic Detectors, Cameras, and Systems*, C. B. Johnson & E. J. Fenyves, eds., *Proc. SPIE* **2551**, pp. 248-259, 1995.
9. L. G. Smeins, E. H. Cole, J. M. Stechman, G. Lorman, and G. Becker, "STIS 1K x 1K Photon Counting Array Detector System," *Photoelectronic Detectors, Cameras, and Systems*, C. B. Johnson & E. J. Fenyves, eds., *Proc. SPIE* **2551**, pp. 262-272, 1995.
10. C. L. Joseph, R. Bybee, and V. Argabright, "Stability coefficients for the multianode microchannel array system," *Rev. Sci. Instrum.* **69**, No. 4, pp. 1898-1905, 1998.
11. V. S. Argabright, S. Franka, P. Frank, G. A. Lorman, C. N. Van Houten, J. Abraham, R. L. Bybee, C. L. Joseph, B. E. Woodgate, R. A. Kimble, and A. C. Danks, "Photometric stability of the STIS MAMA detectors," *Space Telescopes and Instruments V*, P. Y. Bely & J. B. Breckinridge, eds., *Proc. SPIE* **3356**, pp. 389-400. 1998.
12. D. B. Kasle, "Decoding techniques for fine-fine geometry multi-anode microchannel arrays," *Ultraviolet Technology II*, *Proc. SPIE* **932**, pp. 280-284, 1988.
13. D. B. Kasle and J. S. Morgan, "High resolution decoding of Multi-Anode Microchannel Array detectors," *EUV, X-ray, and gamma-ray instrumentation for astronomy II*, *Proc. SPIE* **1549**, pp. 52-58, 1991.
14. G. Sonneborn et al., "Spatially Resolved STIS Spectroscopy of SN1987A: Evidence for Shock Interaction with Circumstellar Gas," *ApJ* **492**, pp. L139-L142, 1998.
15. J. B. Hutchings et al., "Gas Cloud Kinematics Near the Nucleus of NGC 4151," *ApJ* **492**, pp. L115-L119, 1998.
16. S. R. Heap, G. M. Williger, A. Smette, I. Hubeny, M. S. Sahu, E. B. Jenkins, T. M. Tripp, and J. N. Winkler, "STIS Observations of He II Gunn-Peterson Absorption Toward Q 0302-003," *ApJ*, submitted, 1999.
17. J. Clarke, Press release, January, 1998, *http://oposite.stsci.edu/pubinfo/pr/1998/04/04.html.*
18. J. Trauger, Press release, January, 1998, *http://oposite.stsci.edu/pubinfo/pr/1998/05/05.html.*
19. T. M. Brown, C. W. Bowers, R. A. Kimble, A. V. Sweigart, and H. C. Ferguson, "Detection and Photometry of Hot Horizontal Branch Stars in the Core of M32," *Ap. J.*, submitted, 1999.
20. K. Sahu et al., *STIS Instrument Handbook version 3.0*, STScI, Baltimore, 1999.
21. N. R. Walborn and R. C. Bohlin, "Sensitivity Monitor Report for the STIS First-Order Modes," *STIS Instrument Science Report 98-27*, STScI, Baltimore, 1998.
22. C. Bowers et al., "The On-orbit Optical Performance of the Space Telescope Imaging Spectrograph," *Space Telescopes and Instruments V*, P. Y. Bely & J. B. Breckinridge, eds., *Proc. SPIE* **3356**, pp. 401-414. 1998.
23. T. Brown, "Low frequency flat fields for the STIS MAMAs," *STIS IDT Post-Launch Quick-Look Analysis Report #054*, 1998, *http://hires.gsfc.nasa.gov/stis/postcal/quick_reports/r054/r054.html.*
24. M. E. Kaiser, R. C. Bohlin, D. J. Lindler, R. L. Gilliland, V. S. Argabright, and R. A. Kimble, "STIS Signal-to-Noise Capabilities in the Ultraviolet," *PASP* **110**, pp. 978-990, 1998.
25. J. P. Gardner et al., "The Hubble Deep Field South - STIS Imaging," *A. J.*, submitted, 1999.
26. E. B. Jenkins, "A study of near-UV MAMA dark rates: Modeling and predictions," *STIS IDT internal memorandum*, 1997.